Nuclear Science and Techniques (2024) 35:131
https://doi.org/10.1007/s41365-024-01500-7

Construction and performance test of charged particle detector array for MATE

Xiao-Bin Li[1,2] · Long-Hui Ru[1,2] · Zhi-Chao Zhang[1,2] · Bing-Feng Lv[1,2] · Ning-Tao Zhang[1,2] · Jin-Long Zhang[1,2] · Chen-Gui Lu[1,2] · Bing-Shui Gao[1,2] · Jun-Bing Ma[1,2] · Fu-Shuai Shi[1,2] · Satoru Terashima[1,3,4] · Xiao-Dong Xu[1,2] · Zhen Bai[1] · Shi-Wei Xu[1] · Yan-Yun Yang[1,2] · Hooi-Jin Ong[1,2,3,4,5] · Xiao-Dong Tang[1,2,5]

Received: 13 March 2024 / Revised: 31 March 2024 / Accepted: 21 April 2024 / Published online: 21 July 2024

Abstract
A charged particle array named MATE-PA, which serves as an auxiliary detector system for a Multi-purpose Active-target Time projection chamber used in nuclear astrophysical and exotic beam Experiments (MATE), was constructed. The array comprised of 20 single-sided strip-silicon detectors covering approximately 10% of the solid angle. The detectors facilitated the detection of reaction-induced charged particles that penetrate the active volume of the MATE. The performance of MATE-PA has been experimentally studied using an alpha source and a 36-MeV ^{14}N beam injected into the MATE chamber on the radioactive ion beam line in Lanzhou (RIBLL). The chamber was filled with a gas mixture of 95% ^{4}He and 5% CO_2 at a pressure of 500 mbar. The results indicated good separation of light-charged particles using the forward double-layer silicon detectors of MATE-PA. The energy resolution of the Si detectors was deduced to be approximately 1% (σ) for an energy loss of approximately 10 MeV caused by the α particles. The inclusion of MATE-PA improves particle identification and increases the dynamic range of the kinetic energy of charged particles, particularly that of the α particles, up to approximately 15 MeV.

Keywords Silicon detector array · Active target · Time projection chamber

1 Introduction

Advances in techniques for providing radioactive isotope (RI) beams and the construction of high-intensity heavy-ion accelerator facilities [1–5] have opened vast opportunities for experimentally studying and understanding nuclei far from the beta-stability line [6–8], as well as nuclear reactions relevant to astrophysics. In experiments involving reaction targets, the selection an appropriate material, phase (solid, liquid, or gas), and thickness for target is crucial to ensure adequate luminosity and achieve the intended physical goals. The rates of RI beams are usually several orders of magnitude lower than those of stable beams for nuclear spectroscopy, wherein charged particles are measured. Hence, employing sufficiently thick reaction targets while attaining moderate energy resolution is crucial. However, such requirements are usually difficult to fulfill with ordinary solid or liquid targets because the uncertainties in reaction vertices and energy straggling impair the resolution.

An active-target time projection chamber (TPC) [9, 10] with a typical reaction gas thickness of 10–100 mg/

This work was partially supported by the National Natural Science Foundation of China (Nos. 12175280 and 12250610193), and the National Key R & D Program of China (No. 2016YFA0400500). H. J. Ong and X. D. Xu acknowledges the support of the CAS "Light of West China" Program. Z. C. Zhang acknowledges the support of the Natural Science Foundation of Gansu (No. 23JRRA676).

✉ Zhi-Chao Zhang
zhangzc@impcas.ac.cn

✉ Ning-Tao Zhang
zhangningtao@impcas.ac.cn

✉ Hooi-Jin Ong
onghjin@impcas.ac.cn

1 Institute of Modern Physics (IMP), Chinese Academy of Sciences, Lanzhou 730000, China

2 School of Nuclear Science and Technology, University of Chinese Academy of Sciences, Beijing 100049, China

3 Research Center for Nuclear Physics, Osaka University, Ibaraki, Osaka 567-0047, Japan

4 RIKEN Nishina Center, Wako, Saitama 351-0198, Japan

5 Joint Department for Nuclear Physics, Lanzhou University and Institute of Modern Physics, Chinese Academy of Sciences, Lanzhou 730000, China

cm^2 provides the high luminosity necessary for nuclear spectroscopy using RI beams, with little or moderate loss of resolution. Because the reaction gas in an active-target TPC also serves as a detector medium, the reaction vertices of the reaction-induced charged particles can be determined by tracking the TPC. Because of these advantages, active-target TPC scores [11–19] have been established for experiments [20–23] with RI beams. Recently, a prototype active-target TPC with 1024 channel readouts, named the Multi-purpose Active-target Time projection chamber for nuclear astrophysical and exotic beam Experiments (MATE-1000) [24], was developed at the Institute of Modern Physics of the Chinese Academy of Sciences (IMP-CAS). This innovative system was applied to measure the $^{12}C+^{12}C$ fusion reaction at stellar energy levels [24] and energies above the Coulomb barrier [25]. Building on earlier success, a larger version of MATE with approximately 4000 channel readouts, hereafter denoted as MATE-4000, was constructed. The sensitive volume of the MATE-4000 was 300(L)×300(W)×200(H) mm^3. To detect the reaction-induced charged particles that penetrate the MATE active volume, a charged particle detector array, called the MATE Particle detector Array (MATE-PA), consisting of 20 single-sided strip silicon detectors, was designed and constructed. The MATE-4000 software (Fig.1a) has been configured using a ^{14}N beam incident on ^4He and employed in experiments to measure the inelastic alpha scattering of ^{11}C and scrutinize the possible $Z = 6$ magic number [26] on the proton-rich side.

In this paper, we report on the construction and performance tests of the MATE-PA. Section 2 describes the design concept, geometry, and readout electronics of the array. To assess the performance of the detector array, an experiment was conducted using $^{14}N+^4He$-induced reactions. Monte Carlo simulations were performed to estimate the geometrical acceptance of the MATE-PA. The details of the experiment, along with the experimental and simulation results are provided in Sect. 3. Prospects for experiments using MATE-4000 in combination with MATE-PA are also presented. Conclusions and prospects are presented in Sect. 4.

2 Charged particle detector array for MATE

In this section, the design concept and specifications of the MATE-PA are presented. The array is designed to achieve the largest possible angular coverage within MATE-4000. Detailed descriptions of the MATE-4000 and its performance have been provided in a previous paper.

2.1 Detector array

The particle-detector array consists of 20 single-sided strip silicon detectors produced by Hamamatsu Photonics (Serial nos. S10938-6734 and S10938-6735), mounted in a single-layer 2 × 3 matrix on both sidewalls and double-layer 2 × 2 matrix on the front wall of the target chamber. Each silicon detector had eight strips with widths of 11.275 mm, strip gaps of 0.1 mm, and sensitive areas of 91 mm × 91 mm; the size of one silicon detector was 100 mm × 100 mm. The side silicon detectors had nominal thicknesses of 600 μm, while the front and rear forward silicon detectors had thicknesses of 150 μm and 600 μm, respectively. The upper (lower) rows of the right- and left-side silicon detectors were labeled as RU_i (RD_i) and LU_i (LD_i), respectively, where the subscript i indicates 1, 2, or 3. The forward detectors consisted of two layers of Si detectors, labeled FF_j and FS_j, where the subscript j indicates 1, 2, 3, or 4, as shown in Fig. 1b. For simplicity and to reduce the risk of electric discharge, we mounted the silicon detectors close to the flanges. The distance from the RU_i (RD_i) and LU_i (LD_i) Si detectors to the field cage was set as 13.35 cm (14.00 cm), while that from FF_j (FS_j) to the field cage was set as 17.80 cm (19.15 cm). The silicon detector array covered approximately 10.6% of the total (4π) solid angle in the laboratory frame, on the assumption that the reaction point was at the center of the TPC.

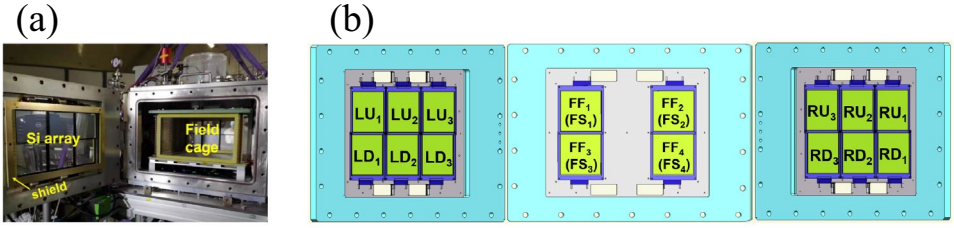

Fig. 1 (Color online) (**a**) Side view of MATE-4000 with the constructed silicon detector array. The TPC field cage (sensitive area) is placed at the center of the chamber, with 20 silicon detectors mounted on the flanges around it. (**b**) Layout of the silicon detector array, as seen from the beam direction. The side flanges have been tilted for clarity. See text for detailed descriptions of the assignments

Strip silicon detectors with moderately large strip widths were chosen instead of large-area single-channel or micro-strip silicon detectors is to achieve sufficient energy resolution while maintaining a manageable number of readout channels. The current strip width is sufficient because the silicon detector array will be used together with the TPC, which can provide track information, and the maximum rate of particles hitting the silicon detectors is expected to be of the order of a few hundred particles per second.

To protect the Si detectors from possible electric discharges, an electrostatic shield layer (Fig.1a) was placed between the MATE field cage and each side of the Si array. The shields were fabricated by soldering Cu-Be wires with diameters of 100 µm at a constant distance of 1 cm on the copper-clad surface of a glass epoxy frame. Electrical grounding was achieved by connecting the shields to a vacuum chamber. Because no electric discharge was observed during the commissioning experiment, the distances were optimized for future experiments to improve geometrical acceptance. For instance, the geometrical acceptance can be increased by approximately two times by reducing the distance between the silicon detectors and field cage from the current distance of approximately 15 cm to 5 cm.

2.2 Electronics and data acquisition system

The output signals of the silicon detectors were fed into 16-channel integrated charge-sensitive preamplifiers, designed by the China Institute of Atomic Energy. The pre-amplifier, named the smart preamplifier (SPA) [27], was designed as a compact and low-cost preamplifier with a fast response and low power consumption. Its smaller volume allows it to be placed closer to the detectors, leading to a reduction in the environmental noise and the achievement of a performance similar to that of other commercial preamplifier modules. Owing to the limited space in the MATE chamber, the SPA modules were mounted outside the flanges.

Every 16 readout signals from the SPA module were fed to a Mesytec MSCF-16 module before being fed to an analog-to-digital converter (ADC; Mesytec MADC-32 module). The Mesytec MSCF-16 module included 16-channel shaping and timing filter amplifiers, along with constant fraction discriminators. The timing signals from the MSCF-16 modules were sent to a time-to-digital converter (TDC; CAEN V1190A module). A typical electron circuit diagram is presented in Fig. 2. The VME and general electronics for TPC (GET-based data acquisition systems were employed for the data readout from the silicon and TPC detectors, respectively [28, 29]. Because the GET system acquires at a much slower rate (approximately 100 Hz for MATE), only reaction events were selected to trigger GET

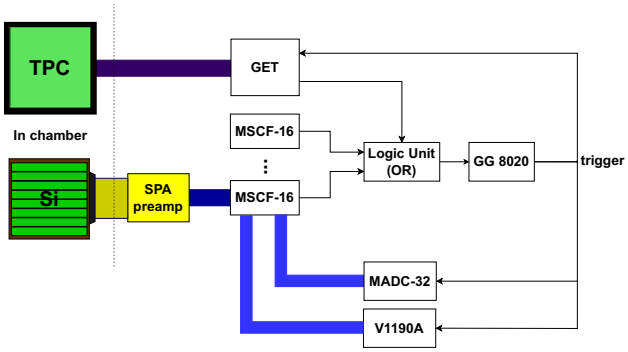

Fig. 2 (Color online) Typical electronic circuit diagram for an Si detector

acquisition. In the current experiment, OR signals from the MSCF-16 modules and GET system were fed to a gate generator (ORTEC GG8020) to provide gate signals for the VME and GET systems. Therefore, both DAQ devices started simultaneously and operated at the same rate.

3 Experiment

To evaluate the performance of the Si detector array, we performed an experiment at the RIBLL [30, 31] and at the heavy ion research facility in Lanzhou (HIRFL) [32, 33], operated by the IMP-CAS. A ^{14}N primary beam with an energy of 117.6 MeV provided by a sector focusing cyclotron (SFC) was transported to the RIBLL. To reduce the energy of ^{14}N and stop it in the TPC chamber, Al plates with thicknesses of 39.2 and 60.6 μm were placed at the momentum-dispersive focal plane C1 and final achromatic focal plane T2, respectively. The resulting ^{14}N beam, with a total energy of about 36 MeV and an intensity of 10^5 pps, was injected into the gas chamber of the TPC, which was filled with a gas mixture of 95% ^{4}He and 5% CO_2 at 500 mbar. The gas mixture served as both the target and detection medium. Charged particles generated by reactions between ^{14}N and the target nuclei were tracked and detected by the TPC. Some of the charged particles that penetrated the TPC were detected by the Si detectors. The data was primarily obtained using a Si $\bigcup$ TPC trigger. To prevent the beam from triggering the TPC, the TPC sensitive area was divided into two regions: low- and high-gain regions. The low-gain region had a width of $\pm$1.7 cm around the beam axis for the detection of beam particles, and high-gain regions were located on both sides for the detection of reacted particles and TPC trigger generation.

For simplicity, the outputs of every four neighboring channels of the Si detectors on the left and right sides were summed into one channel, thereby reducing the number of electronic readout channels without significantly affecting

the energy resolution. All the Si detectors were energy calibrated using a triple-nuclide alpha source consisting of ^{239}Pu (5.147 MeV), ^{241}Am (5.486 MeV), and ^{244}Cm (5.805 MeV), prior to the experiment. The typical energy resolution (σ) was approximately 0.8% at an alpha particle energy of 5.5 MeV.

3.1 Particle identification

3.1.1 Forward region

Reaction-induced charged particles emitted in the forward direction were detected using FF and FS silicon detectors. Figure 3a shows the typical particle identification plot obtained from the measured energy deposited in the first (ΔE_{FF}) and second layers (ΔE_{FS}) of the forward silicon detectors. Three different loci corresponding to protons, deuterons, and α particles were clearly observed. We eliminated overflow events and events caused by accidental triggers by considering the tracking information from the TPC.

To better understand the data, simulations using the MATEROOT program [34] were performed by assuming ^{4}He(^{14}N, p), ^{4}He(^{14}N, d), and ^{4}He(^{14}N, α) reactions and considering the full geometry of the detector setup, incident ^{14}N beam energy, and ^{4}He + CO_2 gas mixture in the TPC chamber. MATEROOT is a FairRoot [35]-based data analysis and simulation platform built, on CERN's open-source data analysis software ROOT [36] and the GEANT4 simulation framework [37], developed specifically for experiments with MATE. The simulation results (green) are compared with the experimental data (blue) in Fig. 3a. Deviations between the experimental and simulation data were observed, and they were attributed to the insufficient energy calibration and inappropriate extrapolation along the energy-deposit axes. To eliminate these deviations, we considered the turnaround points of proton loci, which correspond to protons that penetrate the second-layer silicon, in addition to the triple-alpha-source data. The turnaround point was determined by searching for the crossing between the two curves obtained by fitting the loci of the protons that penetrated and stopped in the second-layer silicon. Four data points, which included the turnaround point and three data points from the triple-alpha source data, were used to recalibrate the energy-deposit axes. The resulting experimental loci after recalibration and simulation data are shown in Fig. 3b. The energy resolution of the Si detectors was deduced to be approximately 1% (σ) for an energy loss of approximately 10 MeV caused by the α particles. The results demonstrated sufficient particle identification for light-charged particles. To further discriminate protons from the energetic deuterons that punch through both silicon layers, the second-layer silicon must be replaced with a thicker detector such as CsI(Tl) or gadolinium aluminium gallium garnet (GAGG).

3.1.2 Side region

Under the current experimental conditions, most of the light-charged particles that penetrated the TPC and headed towards the side silicon detectors stopped in the single-layer silicon detectors. Figure 4 shows a typical scattering event recorded by a detector. The z axis in Fig. 4a is defined as the beam axis, whereas the y axis is defined perpendicular to the beam direction. $z = 0$ cm represents the upstream side of the field cage or entrance of the TPC region sensitive to the incident beam. The rectangles at the top and two sides of the figure represent the silicon detector strips. The same event in the x (drift direction)-z plane is shown in Fig. 4b. The recoil α particles and residual ^{14}N particles were observed simultaneously; the α particles penetrated the TPC sensitive area and hit the highlighted group of strips (yellow), whereas the ^{14}N particles stopped in the sensitive area. The charge and track information of the incident ^{14}N beam particles were not recorded for this reaction because of the space-charge effect in the low-gain beam region.

For these events, particle identification (PID) can be performed using the charge (ΔE_{TPC}) and track length

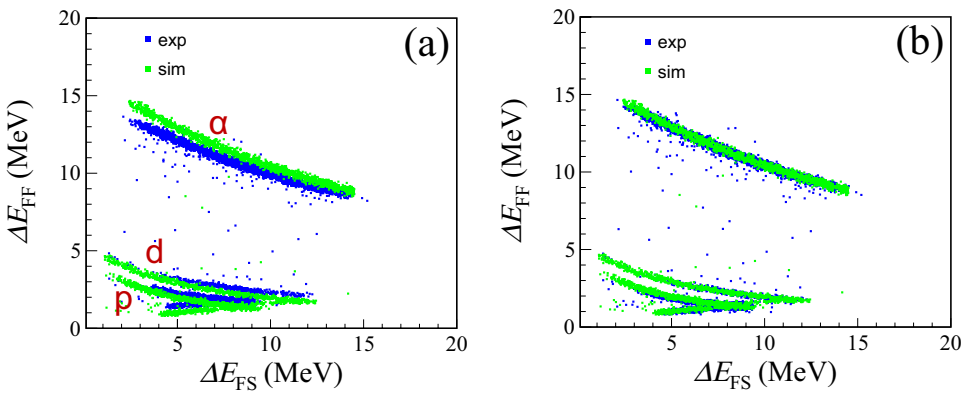

Fig. 3 (Color online) (**a**) ΔE-ΔE plot of the charged particles induced by the ^{4}He+^{14}N reaction, obtained via the forward silicon detectors. Blue and green points represent experimental and simulated data, respectively. The axes are calibrated using a triple-nuclide α source. (**b**) ΔE-ΔE plot after re-calibration, considering the penetration point of protons

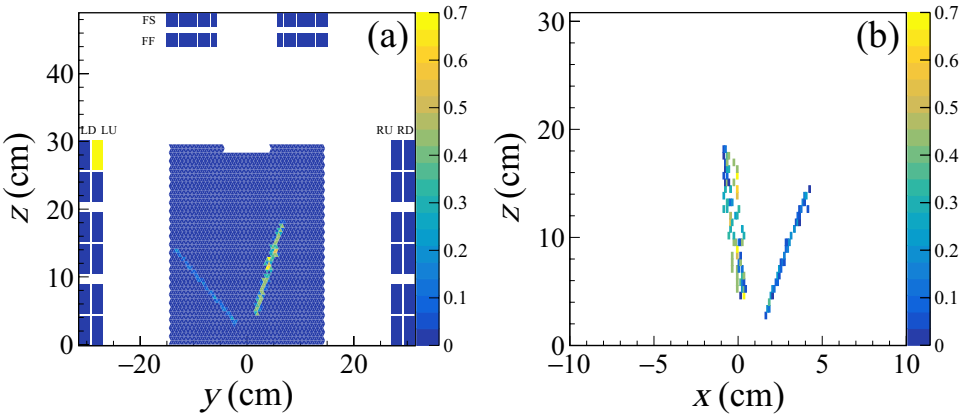

Fig. 4 (Color online) Trajectory of a typical scattering event on the (**a**) anode pad (y-z) plane and (**b**) drift (x-z) plane. The z axis is along the beam direction

(denoted as L) obtained via the TPC and energy deposited in the side silicon detectors (ΔE_{Si}). The ΔE_{TPC} values were calibrated using the energy-loss curves simulated using the GEANT4 program. Typical ΔE_{TPC}-L and ΔE_{TPC}-$\Delta E_{\mathrm{Si+TPC}}$ scatter plots are shown in Fig. 5. For a clearer identification of the light and heavy particles, the ΔE_{TPC} axes of the PID plots are shown on a logarithmic scale.

Raw data plotted without the response of the front silicon detector are shown in Fig. 5a and b, where the two main components can be identified as particles with atomic number $Z > 2$ and light particles with $Z \leq 2$. In Fig. 5a, the expected light-charged particles with relatively high energy penetrated the TPC sensitive area from approximately 10 to 28 cm depending on the emitted angles, and some of them were detected by the side silicon detector, as shown in Fig. 5b.

The background can be mainly attributed to the electronic noise of the TPC and possible electrons induced by the beam particles within the beam region around the center of the TPC-sensitive area, along the beam direction. The electronic noise of the TPC can be eliminated by limiting the number of hits on the anode pad (e.g. $10 \leq N_{\mathrm{hits}} \leq 200$) of the TPC.

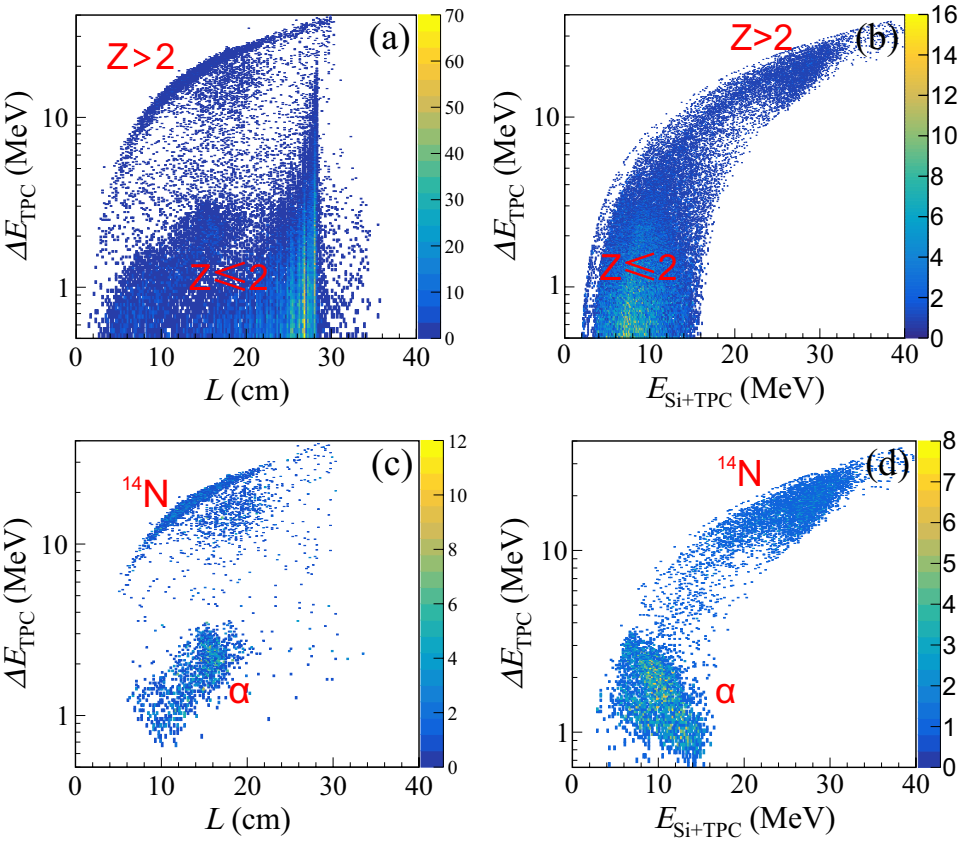

Fig. 5 (Color online) (**a**) Scattering plot of the collected charge versus length of the charged particles in the TPC (L). (**b**) ΔE-E plot for ^{14}N and α particles, measured with the TPC (ΔE_{TPC}) and silicon detector (ΔE_{Si}). (**c**) and (**d**) Similar plots after applying various conditions such as the number of hits on the TPC anode pad and geometrical conditions. For details, see text

The electrons induced by the beam particles can be filtered out by applying geometrical constraints based on the kinematics of the two-body reaction, that is, by positioning the first and last points of the trajectories within the high-gain region and selecting appropriate track angles and directions for the two particles. A typical "good" event is shown in Fig. 4. A clear PID plot was obtained after applying the aforementioned conditions, as shown in Fig. 5c and d. The backgrounds, especially the low ΔE_{TPC} components, were removed, resulting in a clear separation between ^{14}N and the α particles. For the α particles that stopped in the TPC, as shown in Fig. 5c, energies as low as a few hundred keV were detected, consistent with the MATE-1000 results [24]. Owing to the MATE-PA, the detection energy range was extended to approximately 15 MeV for α particles, as shown in Fig. 5d. In this experiment, protons and deuterons were barely detected owing to the insufficient gain of the TPC. The clump below the ^{14}N band, at approximately $L = 20$ cm in Fig. 5a and c, is due to a malfunctioning channel in the GET electronics, which quenched the collected charges in a region close to the beam.

The results demonstrated the feasibility of identifying and separating the scattered light particles and residual heavy particles using the MATE-PA, incorporating the tracking information obtained with the TPC. Owing to the tracking information, the angles of the particles were also extracted as shown in Fig. 6, which can be useful for further analyses to refine particle identification.

For low-energy charged particles that stop in the TPC, one must rely on the range information for particle identification. Another good alternative is to insert the TPC into a solenoid or dipole magnet and identify the particles based on their curved paths in a magnetic field [14].

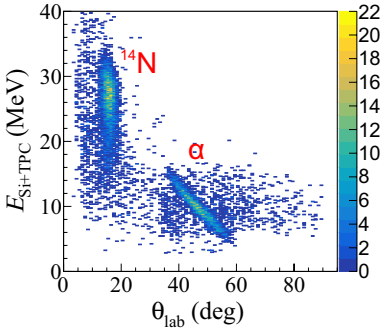

Fig. 6 (Color online) Correlation between the energy deposited in the silicon detectors and angles of the particles obtained from Fig. 5d

3.2 Geometrical acceptance

For experiments that require measurements of absolute differential cross-sections, determining the solid angle or geometrical acceptance of the detectors is crucial. To estimate the geometrical acceptance, simulations using MATEROOT, considering the full geometrical setup, incident beam energy, gas medium, energy deposit of the beam, and reaction-induced charged particles in the detectors, were performed. For thick-target experiments, where the reaction energy changes drastically as the beam particles travel along the TPC, simultaneously iterating the geometrical acceptance simulation by considering the determined differential cross-section is essential. However, for simplicity, we assumed isotropic alpha scattering in this study.

For reactions within a very small range of excitation energies, the geometric acceptance can be represented as a function of the polar angle in a center-of-mass system. The simulated geometrical acceptance of the prototype MATE-PA for ^{14}N+^{4}He elastic scattering is shown in Fig. 7a. Geometrical acceptance (ϵ) is defined as the ratio of silicon responses (total number of responses of 0 or 1 per reaction event) to the number of reaction events generated within a subtended polar angle ($\theta - \Delta\theta$ and $\theta + \Delta\theta$), where θ is the polar angle, and $2\Delta\theta$ is the bin size. Only events in which the TPC that responded to the recoil α particles ($L >$

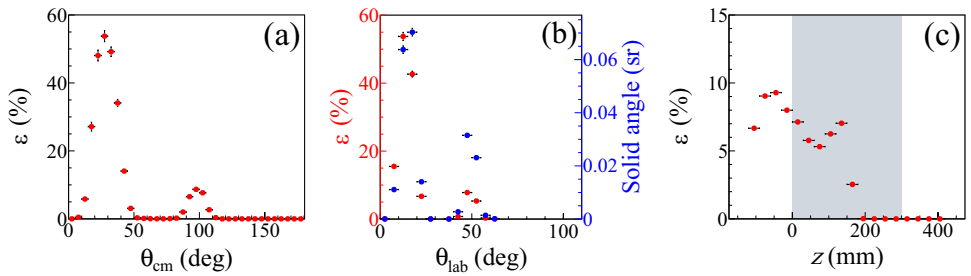

Fig. 7 (Color online) (**a**) Geometrical acceptance (ϵ) of MATE-PA for the α particles induced by the ^{4}He(^{14}N,α)^{14}N reaction at different center-of-mass angles. The ^{14}N beam energy at the entrance of the TPC chamber was about 36 MeV. (**b**) Geometrical acceptance (left axis) and solid angle in unit steradian (right axis) of the Si array at different laboratory angles. (**c**) Geometrical acceptance for different reaction vertex positions along the beam axis. The shaded region represents the TPC sensitive area

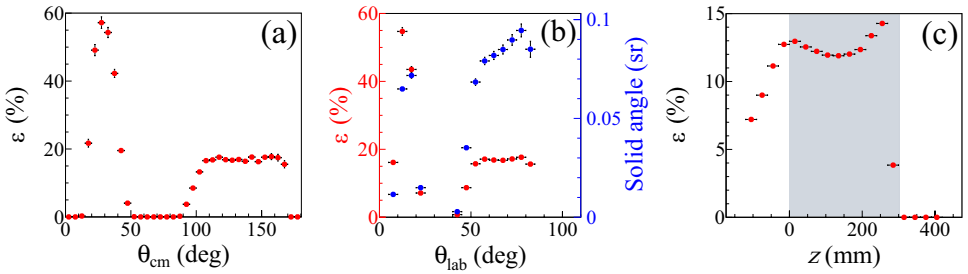

Fig. 8 (Color online) (**a**) Geometrical acceptance (ϵ) of MATE-PA for the α particles induced by the ^{4}He(^{12}C,α)^{12}C reaction at different center-of-mass angles. The ^{12}C beam energy at the entrance of the TPC was about 75 MeV/nucleon. (**b**) Geometrical acceptance (left axis) and solid angle in unit steradian (right axis) of the Si array at different laboratory angles. (**c**) Geometrical acceptance for different reaction vertex positions along the beam axis. The shaded region represents the TPC sensitive area

5 cm) were considered. We assumed a uniform distribution of reaction vertices within the active volume of the TPC, and the reaction region was limited to the domain z = [0, 10] cm. For a more intuitive understanding, the geometrical acceptance and solid angle (in steradian) are shown as functions of the polar angle in the laboratory system in Fig. 7b by the left and right axes, respectively. The angular dependence of the geometrical acceptance primarily arises from the layout of the silicon detectors.

To evaluate the dependence of the geometrical acceptance on the reaction vertex position, we divided the TPC sensitive area into ten parts along the z-axis. For each part of the sensitive area, we obtained an angle-integrated geometric acceptance. The simulated result for the ^{14}N+^{4}He elastic scattering is shown in Fig. 7c, where the shaded region represents the TPC sensitive region.

The average total geometric acceptance was estimated to be approximately 6.0% for the ^{4}He(^{14}N,α)^{14}N reaction. The energy of the ^{14}N beam particles decreased quickly, and no reaction occurred at the end of the sensitive area. This led to a reduction in the overall geometrical acceptance. However, the actual geometrical acceptance was expected to be higher. Based on an analysis of the experimental data, some of the reaction events occurring at the so-called "dead region" between the gas entrance window and field cage were also recorded. Therefore, in the present simulation, the reaction vertex position was expanded from the TPC sensitive area to the entire gas chamber. The results show that the reactions occurring near the front of the TPC sensitive area contribute to a sizable geometrical acceptance. Hence, the MATE and MATE-PA can be used to measure the reactions occurring both within and outside the TPC sensitive area. Moderate resolution can still be achieved with careful track reconstruction and proper track extrapolation. This aspect is useful for thick target experiments that measure the excitation function using a low-energy beam.

For comparison, a simulation was also performed for the elastic alpha scattering of a ^{12}C beam with an energy of 75 MeV/nucleon, incident on a TPC filled with a gas mixture of 95% ^{4}He and 5% CO_2 at a gas pressure of 500 mbar. The results shown in Fig. 8a–c are similar to those shown in Fig. 7. The average total geometrical acceptance was estimated to be about 12.8% from Fig. 8c.

The addition of the MATE-PA increased the dynamic range of the kinetic energy of the charged particles, improved particle identification, and opened up broad opportunities for experiments measuring nucleon-transfer reactions, elastic and inelastic scattering, charged-particle decay, and evaporation.

4 Conclusion and future prospect

A prototype particle detector array consisting of 20 single-sided strip silicon detectors was constructed for use in MATE-4000 to achieve large-angle and wide-energy-range measurements. The detector system was commissioned at the HIRFL-RIBLL, using a 36-MeV, 10^{5}-pps ^{14}N beam incident on MATE-4000, which was filled with a gas mixture of 95% ^{4}He and 5% CO_2 (500 mbar). The test results demonstrate good separation of light-charged particles by the forward double-layer silicon detectors of the MATE-PA. The energy resolution of the Si detectors was deduced to be approximately 1% (σ) for an energy loss of approximately 10 MeV caused by α particles. Combined with the MATE-PA, MATE-4000 can offer significant opportunities for experiments in nuclear astrophysics and RI beam physics in future.

Recently, the readout cables of the MATE-PA have been replaced with Kapton ribbon cables to improve the flexibility and work efficiency. The use of ribbon cables also helps reduce environmental noise. For readout electronics, we used SPA and MSCF modules, incorporating a VME-based ADC for data acquisition. In future, we plan to migrate the GET system, used for the readout of TPC signals. An upgrade

of MATE-PA with additional detectors, such as CsI(Tl) or GAGG, is also under consideration to accommodate a wide variety of experiments.

Acknowledgements The authors thank the accelerator operators for providing stable beams throughout the experiment.

Author's contribution All authors contributed to the study conception and design. Material preparation, data collection and analysis were performed by Xiao-Bin Li, Long-Hui Ru, Zhi-Chao Zhang, Bing-Feng Lv, Ning-Tao Zhang, Jin-Long Zhang, Chen-Gui Lu, Bing-Shui Gao, Jun-Bing Ma, Fu-Shuai Shi, Staoru Terashima, Hooi-Jin Ong, Xiao-Dong Xu, Zhen Bai, Shi-Wei Xu, Yan-Yun Yang, and Xiao-Dong Tang. The first draft of the manuscript was written by Xiao-Bin Li, Zhi-Chao Zhang, Ning-Tao Zhang, and Hooi-Jin Ong, and all authors commented on previous versions of the manuscript. All authors read and approved the final manuscript.

Data availibility The data that support the findings of this study are openly available in Science Data Bank at https://cstr.cn/31253.11.sciencedb.j00186.00145 and https://doi.org/10.57760/sciencedb.j00186.00145.

Declarations

Conflict of interest The authors declare that they have no Conflict of interest.

References

1. H. Geissel, H. Weick, M. Winkler et al., The Super-FRS project at GSI. Nucl. Instrum. Meth. B **204**, 71–85 (2003). https://www.sciencedirect.com/science/article/pii/S0168583X02018931
2. D. Morrissey, Status of the FRIB project with a new fragment separator. J. Phys. Conf. Series **267**, 012001 (2011). https://doi.org/10.1088/1742-6596/267/1/012001
3. T. Kubo, D. Kameda, H. Suzuki et al., BigRIPS separator and ZeroDegree spectrometer at RIKEN RI Beam Factory. Prog. Theor. Exp. Phys. **2012**, 03C003 (2012). https://doi.org/10.1093/ptep/pts064
4. L.N. Sheng, X.H. Zhang, J.Q. Zhang et al., Ion-optical design of High energy FRagment Separator (HFRS) at HIAF. Nucl. Instrum. Meth. B **469**, 1–9 (2020). https://doi.org/10.1016/j.nimb.2020.02.026
5. J.C. Yang, J.W. Xia, G.Q. Xiao et al., High intensity heavy ion accelerator facility (HIAF) in China. Nucl. Instrum. Meth. B **317**, 263–265 (2013). https://www.sciencedirect.com/science/article/pii/S0168583X13009877
6. P.G. Hansen, B.M. Sherrill, Reactions and single-particle structure of nuclei near the drip lines. Nucl. Phys. A **693**, 133–168 (2001). https://www.sciencedirect.com/science/article/pii/S0375947401011046
7. T. Nakamura, H. Sakurai, H. Watanabe, Exotic nuclei explored at in-flight separators. Prog. Part. Nucl. Phys. **97**, 53–122 (2017). https://www.sciencedirect.com/science/article/pii/S0146641017300522
8. M. Pfützner, I. Mukha, S.M. Wang, Two-proton emission and related phenomena. Prog. Part. Nucl. Phys. **132**, 104050 (2023). https://www.sciencedirect.com/science/article/pii/S0146641023000315
9. D. Nygren, In *1975 PEP Summer Study*, A Time Projection Chamber: 1975. pp. 126–133 (1975)
10. D. Bazin, T. Ahn, Y. Ayyad et al., Low energy nuclear physics with active targets and time projection chambers. Prog. Part. Nucl. Phys. **114**, 103790 (2020). https://www.sciencedirect.com/science/article/pii/S0146641020300375
11. C.E. Demonchy, W. Mittig, H. Savajols et al., MAYA, a gaseous active target. Nucl. Instrum. Meth. A **573**, 145–148 (2007). https://www.sciencedirect.com/science/article/pii/S0168900206022558
12. S. Ota, H. Tokieda, C.S. Lee et al., CNS active target (CAT) for missing mass spectroscopy with intense beams. Nucl. Chem. **305**, 907–911 (2015). https://doi.org/10.1007/s10967-015-4130-5
13. W. Mittig, S. Beceiro-Novo, A. Fritsch et al., Active Target detectors for studies with exotic beams: Present and next future. Nucl. Instrum. Meth. A **784**, 494–498 (2015). https://www.sciencedirect.com/science/article/pii/S0168900214012054
14. J. Bradt, D. Bazin, F. Abu-Nimeh et al., Commissioning of the active-target time projection chamber. Nucl. Instrum. Meth. A **875**, 65–79 (2017). https://www.sciencedirect.com/science/article/pii/S0168900217309683
15. T. Furuno, T. Kawabata, H.J. Ong et al., Performance test of the MAIKo active target. Nucl. Instrum. Meth. A **908**, 215–224 (2018). https://www.sciencedirect.com/science/article/pii/S0168900218309951
16. E. Koshchiy, G.V. Rogachev, E. Pollacco et al., Texas Active Target (TexAT) detector for experiments with rare isotope beams. Nucl. Instrum. Meth. A **957**, 163398 (2020). https://www.sciencedirect.com/science/article/pii/S0168900220300073
17. J.Y. Xu, L.Q. T., Y.L. Y et al., Performance of a small AT-TPC prototype. Nucl. Sci. Tech. **29**, 263–265 (2018). https://doi.org/10.1007/s41365-018-0437-6
18. L.S. Yang, J.Y. Xu, Q.T. Li et al., Performance of the CAT-TPC based on two-dimensional readout strips. Nucl. Sci. Tech. **32**, 85 (2021). https://doi.org/10.1007/s41365-021-00919-6
19. H.K. Wu, Y.J. Wang, Y.M. Wang et al., Machine learning method for ^{12}C event classification and reconstruction in the active target time-projection chamber. Nucl. Instrum. Meth. A **1055**, 168528 (2023). https://www.sciencedirect.com/science/article/pii/S0168900223005181
20. T. Furuno, T. Kawabata, S. Adachi et al., Neutron quadrupole transition strength in ^{10}C deduced from the ^{10}C(α,α') measurement with the MAIKo active target. Phys. Rev. C **100**, 054322 (2019). https://doi.org/10.1103/PhysRevC.100.054322
21. J. Bishop, C.E. Parker, G.V. Rogachev et al., Neutron-upscattering enhancement of the triple-alpha process. Nat. Commun. **13**, 2151 (2022). https://doi.org/10.1038/s41467-022-29848-7
22. J. Bishop, G.V. Rogachev, S. Ahn et al., First observation of the $\beta 3\alpha p$ decay of ^{13}O via β-delayed charged-particle spectroscopy. Phys. Rev. Lett. **130**, 222501 (2023). https://doi.org/10.1103/PhysRevLett.130.222501
23. S. Giraud, J.C. Zamora, R.G.T. Zegers et al., β^+ gamow-teller strengths from unstable ^{14}O via the $(d,^2$He) reaction in inverse kinematics. Phys. Rev. Lett. **130**, 232301 (2023). https://doi.org/10.1103/PhysRevLett.130.232301
24. Z.C. Zhang, X.Y. Wang, T.L. Pu et al., Studying the heavy-ion fusion reactions at stellar energies using Time Projection Chamber. Nucl. Instrum. Meth. A **1016**, 165740 (2021). https://doi.org/10.1016/j.nima.2021.165740
25. X.Y. Wang, N.T. Zhang, Z.C. Zhang et al., Studies of the 2 α and 3 α channels of the ^{12}C+^{12}C reaction in the range of $E_{\rm c.m.}$=8.9 MeV to 21 MeV using the active target Time Projection Chamber. Chin. Phys. C **46**, 104001 (2022). https://doi.org/10.1088/1674-1137/ac7a1d
26. D.T. Tran, H.J. Ong, G. Hagen et al., Evidence for prevalent Z = 6 magic number in neutron-rich carbon isotopes. Nat. Commun. **9**, 1594 (2018). https://doi.org/10.1038/s41467-018-04024-y
27. D.X. Wang, C.J. Lin, L. Y et al., Compact 16-channel integrated charge-sensitive preamplifier module for silicon strip

detectors. Nucl. Sci. Tech. **31**, 48 (2020). https://doi.org/10.1007/s41365-020-00755-0
28. J. Giovinazzo, T. Goigoux, S. Anvar et al., GET electronics samples data analysis. Nucl. Instrum. Meth. A **840**, 15–27 (2016). https://doi.org/10.1016/j.nima.2016.09.018
29. E.C. Pollacco, G.F. Grinyer, F. Abu-Nimeh et al., GET: a generic electronics system for TPCs and nuclear physics instrumentation. Nucl. Instrum. Meth. A **887**, 81–93 (2018). https://doi.org/10.1016/j.nima.2018.01.020
30. Z.Y. Sun, W.L. Zhan, Z.Y. Guo et al., Separation and Identification of Isotopes Produced from ^{20}Ne+Be Reaction by Radioactive Ion Beam Line in Lanzhou. Chin. Phys. Lett. **15**, 790 (1998). https://doi.org/10.1088/0256-307X/15/11/004
31. Z.Y. Sun, W.L. Zhan, Z.Y. Guo, RIBLL, the radioactive ion beam line in Lanzhou. Nucl. Instrum. Meth. A **503**, 496–503 (2003). https://doi.org/10.1016/S0168-9002(03)01005-2
32. J.W. Xia, W.L. Zhan, B.W. Wei et al., The heavy ion cooler-storage-ring project (HIRFL-CSR) at Lanzhou. Nucl. Instrum. Meth. A **488**, 11–25 (2002). https://doi.org/10.1016/S0168-9002(02)00475-8
33. W.L. Zhan, H.S. Xu, Z.Y. Sun et al., Present status of HIRFL In Lanzhou. Int. J. Mod. Phys. E **15**, 1941–1956 (2006). https://doi.org/10.1142/S0218301306005526
34. L. Li, Z.C. Zhang, N.T. Zhang et al., MATEROOT: A Simulation and Analysis Tool for Experiments with MATE, in preparation.
35. M. Al-Turany, D. Bertini, R. Karabowicz et al., The fairroot framework. J. Phys. Conf. Series **396**, 022001 (2012). https://doi.org/10.1088/1742-6596/396/2/022001
36. R. Brun, F. Rademakers, ROOT — An object oriented data analysis framework. Nucl. Instrum. Meth. A **389**, 81–86 (1997). https://www.sciencedirect.com/science/article/pii/S016890029700048X
37. S. Agostinelli, J. Allison, K. Amako et al., Geant4—a simulation toolkit. Nucl. Instrum. Meth. A **506**, 250–303 (2003). https://www.sciencedirect.com/science/article/pii/S0168900203013688